# On the Compressible High-Speed Flow Analysis of a Tapered Slab Rocket Motor

Andre B. Salles* and Joseph Majdalani†
*Auburn University, Auburn, AL 36849*

**This work presents a closed-form analytical solution for the compressible, high-speed Taylor motion in an idealized slab rocket motor with a tapered grain. The analysis builds upon the planar mean flow profile in a rectangular channel with porous and slightly tapered walls, extending the incompressible rotational framework to incorporate dilatational effects at elevated Mach numbers. Using sequential perturbations that apply the Rayleigh-Janzen asymptotic technique following a regular expansion in the sine of the taper angle, the inviscid, steady, two-dimensional isentropic flow equations are perturbed in powers of the injection Mach number squared. The resulting expansion enables us to derive closed-form expressions for the velocity, pressure, density, and vorticity distributions. At low Mach numbers, the corresponding profiles are shown to be reducible to the incompressible Taylor solution in a tapered chamber; at higher speeds, they systematically capture the steepening of axial velocity gradients and the axial attenuation of compressibility-induced distortions. Our findings showcase the importance of accounting for the effects of solid propellant grain taper and flow dilatation, as neglecting these perturbations to the flow can lead to erroneous predictions in ballistic codes.**

## Nomenclature

Subscripts and Symbols

| | |
|---|---|
| 00 | leading-order term, $O(1)$ |
| 10 | first taper correction, $O(\epsilon)$ |
| 01 | first compressibility correction, $O(M^2)$ |
| 11 | combined taper–compressibility correction, $O(\epsilon M^2)$ |
| 02 | second compressibility correction, $O(M^4)$ |
| $s$ | quantity evaluated at the propellant surface |
| $\bar{}$ | dimensional quantity |
| $p$ | pressure |
| $(u, v)$ | velocity components in axial and wall-normal directions |
| $(x, y)$ | axial and wall-normal coordinates |

*Greek*

| | |
|---|---|
| $\alpha$ | wall taper angle |
| $\beta$ | ratio of maximum to mean velocity at a given axial station |
| $\gamma$ | ratio of specific heats |
| $\epsilon$ | small taper parameter, $\sin\alpha$ |
| $\eta$ | similarity coordinate, $\beta_{00}\, y/y_s$ |
| $\psi$ | stream function |
| $\Omega$ | vorticity |
| $\rho$ | density |
| $\nabla$ | gradient of |

## I. Introduction

SOLID rocket motors (SRMs) stand among the most widely used chemical propulsion systems due to their structural simplicity, reliability, cost-effectiveness, and ease of manufacturing. Their compact and robust design makes them ideal for a broad range of applications, and these range from educational models to tactical and strategic missiles, as well as launch vehicles. A critical component in the development and design of SRMs consists of the accurate prediction

*Undergraduate Research Assistant, Department of Aerospace Engineering, AIAA University Member 1923947.
†Professor and Francis Chair, Department of Aerospace Engineering, Lifetime Fellow AIAA 199546

of ballistic performance; the latter may be deduced from fundamental parameters such as the chamber pressure, thrust magnitude, and burn duration. Evaluating these performance metrics with a sufficient degree of precision remains essential to ensuring that the motor under consideration meets or exceeds its intended operational goals, payload delivery objectives, and flight trajectory.

From both a design and economic standpoint, the ability to accurately predict ballistic performance may be viewed as being vital. On the design side, for example, it enables us to precisely tailor motor performance to mission requirements. On the economic side, it enables us to minimize the need for costly experimental testing and dependence on extensive static and live firings. In this vein, the advancement of robust and efficient tools for ballistic modeling and simulation may be regarded as being indispensable in the development cycle of SRMs.

One of the most essential elements in the performance of SRMs consists of a suitable grain geometry. More specifically, the internal configuration of the propellant grain perforation plays a key role in prescribing the evolution of the burning surface area over time, thereby shaping the pressure-time and thrust-time profiles. Modern SRMs are typically manufactured with small tapers that reduce the contact between the casting mandrels and the propellant during mandrel removal. The small, divergent angles aid in the reduction of shear stress on the surface of the propellant. This minor design modification minimizes the likelihood of propellant tearing, cracking, and debonding. Tapers are also used to shape the thrust time curve and to soften thrust transients at tail-off. As a result, tapers are often used in high-speed interceptor vehicles requiring thrust curve modifications. Tapers also minimize erosive burning effects and maximize volumetric loading fractions while helping to increase the port-to-throat area ratio.

Among geometric refinements used in contemporary motors, Clayton [1] stands, perhaps, among the first to demonstrate that neglecting small taper angles can produce substantial discrepancies in predicted pressure drop for injection-driven internal flows used to model the bulk gaseous motion in SRMs. In fact, the theoretical foundations for injection-driven internal flows in rocket motors can be traced to the seminal analyses of Taylor [2] and Culick [3]. On the one hand, Taylor furnishes a similarity solution for incompressible flow in a porous rectangular channel, while, on the other hand, Culick extends the framework to rotational flow in axisymmetric (cylindrical) geometries that are germane to solid propellant motors. These solutions, though inviscid, capture the essential vorticity generation induced by wall injection and remain widely used in both analytical investigations and ballistic codes. Clayton [1] subsequently shows, through a regular perturbation treatment of tapered chambers, that the classical Culick profile may be recovered in the zero-taper limit, thereby establishing a systematic means of incorporating grain surface divergence.

Further refinement of this problem is later achieved by Saad et al. [4]; therein, a regular perturbation technique is used to obtain a two-term incompressible solution for tapered slab motors. Corresponding results help to ascertain that pressure-drop predictions based solely on the Taylor or Culick profiles may overestimate chamber pressure losses by as much as 25% to 80%, thereby establishing the necessity of including taper corrections. In parallel, Maicke and Majdalani [5] manage to extend Taylor's planar model to account for compressibility effects through the Rayleigh–Janzen perturbation expansion. In this manner, by expanding the governing equations in even powers of the injection Mach number, a two-term compressible correction is obtained that preserves the overarching rotational structure while capturing dilatational steepening of axial velocity gradients.

Although taper and compressibility corrections have thus been developed independently, a unified analytical formulation that simultaneously accounts for both effects remains absent from the literature. Such a formulation becomes especially pertinent in high-speed motors where elevated injection Mach numbers coexist with slight geometric divergence. The present work addresses this need by combining the small-taper correction with the Rayleigh–Janzen expansion in the Mach number squared.

The Rayleigh–Janzen technique, originating in the early compressible-flow studies of Janzen [6] and Rayleigh [7], requires all dependent variables to be expanded in even powers of the Mach number. Its application to internal injection-driven flows has proven particularly advantageous because it is not restricted by the chamber aspect ratio; moreover, it remains valid provided that the injection Mach number $M$ is sufficiently small, namely, a condition that is typically satisfied in practical SRM operation [8–10]. Unlike slender-body or pseudo-one-dimensional approximations, the present approach retains the fully two-dimensional structure of the vorticity–streamfunction formulation.

By superposing the $\epsilon$-expansion associated with the small taper angle used by Saad et al. [4] and the $M^2$-expansion inherent to the Rayleigh–Janzen method [11], we will systematically pursue closed-form expressions for the streamfunction, velocity components, pressure, density, and vorticity fields. On the one hand, at low speeds, the solution will be shown to be reducible, as a limiting case, to the incompressible Taylor profile in a tapered chamber. On the other hand, higher-order terms will enable us to quantify the progressive steepening of velocity gradients, the axial redistribution of pressure, and the convective transport of compressibility-induced distortions.

## II. Problem Formulation

Following the approach undertaken by Saad et al. [4], we consider the idealized model of a tapered slab rocket motor with porous walls that are oriented at a small angle $\alpha$. This configuration is illustrated in Fig. 1. In this model, the chamber consists of a nontapered section of length $L_0$, height $2h_0$, and width $w_0$, wherein the combustion products are uniformly injected normal to the propellant surface at a constant speed $U_w$. This idealization deliberately overlooks density fluctuations at the burning surface, as well as potential defects or erosive effects in the propellant grain; nonetheless, it remains a widely accepted approximation in the modeling of internal SRM flowfields [5]. Furthermore, the analysis assumes a steady, inviscid, compressible, and adiabatic flow of a calorically perfect gas.

### A. Normalization of Governing Equations

It is prudent to normalize the fundamental variables of interest at the forefront of the analysis. To do so, we let:

$$x = \frac{\overline{x}}{h_0}; \quad y = \frac{\overline{y}}{h_0}; \quad L = \frac{L_0}{h_0}; \quad \nabla = h_0\overline{\nabla}; \quad u = \frac{\overline{u}}{U_w}; \quad v = \frac{\overline{v}}{U_w}; \tag{1}$$

$$p = \frac{\overline{p}}{p_0}; \quad \rho = \frac{\overline{\rho}}{\rho_0}; \quad \psi = \frac{\overline{\psi}}{U_w \rho_0 h_0}; \quad \boldsymbol{\Omega} = \frac{\overline{\boldsymbol{\Omega}}_{h_0}}{U_w}. \tag{2}$$

These relations may be first substituted into the vorticity definition wherein the two velocity components are eliminated in favor of the streamfunction to ultimately produce

$$\frac{\partial^2 \psi}{\partial x^2} + \frac{\partial^2 \psi}{\partial y^2} = \frac{\nabla\rho \cdot \nabla\psi}{\rho} - \Omega\rho. \tag{3}$$

To solve Eq. (3), the entire right hand side must be determined. The vorticity transport equation may be invoked and written as

$$\nabla \times (\boldsymbol{U} \times \boldsymbol{\Omega}) = \frac{1}{\gamma M^2 \rho^2} \nabla\rho \times \nabla p, \tag{4}$$

where the velocity vector is taken to be $\boldsymbol{U} = u\hat{i} + v\hat{j}$. The momentum equation may then be solved for the pressure from Euler's equation, specifically,

$$\rho\nabla\left[\frac{1}{2\rho^2}(\nabla\psi \cdot \nabla\psi)\right] + \Omega\nabla\psi = -\frac{\nabla p}{\gamma M^2}. \tag{5}$$

Lastly, the assumption of an isentropic motion of a calorically perfect gas enables us to put

$$\rho = p^{\frac{1}{\gamma}}. \tag{6}$$

### B. Analysis of Surface Conditions

At first, it may be instructive to closely examine the incompressible streamfunction and vorticity at the propellant surface. As shown by Saad et al. [4], these can be expressed as

$$\psi_s = x \ \sec(\alpha) + L \tag{7}$$

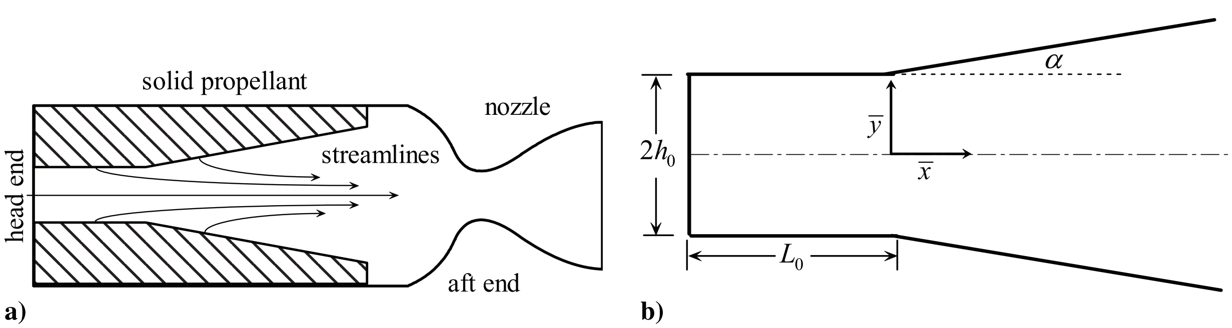


**Fig. 1. Typical slab burner with a) grain taper and b) geometric model used in this study.**

$$y_s = 1 + x\tan(\alpha) \tag{8}$$

$$\Omega_s = \frac{\beta^2\psi_s}{y_s^2}\left[1 - \frac{\psi_s \sin\alpha}{y_s} + \psi_s \cos\alpha \left(\frac{\beta'}{\beta}\right)\right] \tag{9}$$

As shown in Fig. 1, $\beta$ represents a ratio of the peak velocity to the mean velocity at any axial location. The form of $\beta(x)$ is determined in such a way to secure the no-slip boundary condition [4].

### C. Boundary Conditions

We now consider the boundary conditions that accompany the tapered slab problem. Based on Eqs. (7–9), one may recognize the states of the streamfunction and vorticity at the propellant surface, thus giving rise to the conditions prescribed by Eq. (10). By invoking the symmetry condition, wherein the streamfunction and transverse velocity vanish across the midsection plane, and by recognizing that the flow entering the tapered section is a function of the nontapered length, we recover

$$\psi(x, y_s) = \psi_s, \quad \boldsymbol{\Omega}(x, y_s) = \boldsymbol{\Omega}_s \tag{10}$$

$$\psi(x,0) = 0, \quad u(0,y) = \frac{1}{\rho}\frac{\partial\psi}{\partial y}(0,y) = \frac{\pi}{2}L\ \cos(\frac{\pi}{2}y), \quad v(x,0) = \frac{1}{\rho}\frac{\partial\psi}{\partial x}(0,y) = 0. \tag{11}$$

### D. Perturbation Expansion

In accordance with the Rayleigh–Janzen perturbation technique, the variables can be expanded concurrently using the $\epsilon$-$M^2$ double perturbation orders, where $\epsilon = sin(a)$. This may be accomplished by decomposing each variable into leading successive corrections that alternate between $\epsilon$ (first subscript) and $M^2$ (second subscript). In total, we have:

$$\psi(x,y) = \psi_{00}+\epsilon\psi_{10}+M^2\psi_{01}+\epsilon M^2\psi_{11}+O(\epsilon^2, M^4), \quad \boldsymbol{\Omega}(x,y) = \boldsymbol{\Omega}_{00}+\epsilon\boldsymbol{\Omega}_{10}+M^2\boldsymbol{\Omega}_{01}+\epsilon M^2\boldsymbol{\Omega}_{11}+O(\epsilon^2, M^4), \tag{12}$$

$$u(x,y) = u_{00} + \epsilon u_{10} + M^2 u_{01} + \epsilon M^2 u_{11} + O(\epsilon^2, M^4), \quad v(x,y) = v_{00} + \epsilon v_{10} + M^2 v_{01} + \epsilon M^2 v_{11} + O(\epsilon^2, M^4), \tag{13}$$

$$p(x,y) = 1+\epsilon p_{10}+M^2p_{01}+\epsilon M^2p_{11}+M^4p_{02}+O(\epsilon^2, M^6),\ \rho(x,y) = 1+M^2\rho_{01}+\epsilon M^2\rho_{11}+M^4\rho_{02}+O(\epsilon^2, M^6). \tag{14}$$

Furthermore, we expand $\beta(x)$ using

$$\beta(x) = \beta_{00} + \epsilon\beta_{10} + M^2\beta_{01} + \epsilon M^2\beta_{11} + O(\epsilon^2, M^4). \tag{15}$$

At this stage, it is also necessary to expand the thermodynamic variables up to $O(M^4)$, as they remain unaffected at the leading order of $O(1)$. Omitting these higher-order terms would otherwise preclude the establishment of an essential relation between $\Omega$ and $\psi$ that is rather required to determine $\psi$ at $O(M^2)$. Furthermore, $\rho_{01}$ may be deliberately omitted inasmuch as corrections of order $\epsilon$ alone remain incompressible, i.e., providing no tangible contribution to the density field. These expansions are then substituted into the governing equations and systematically segregated by order. In so doing, the vorticity-streamfunction equation recovers

$$O(1): \frac{\partial^2\psi_{00}}{\partial x^2} + \frac{\partial^2\psi_{00}}{\partial y^2} = -\Omega_{00}, \tag{16}$$

$$O(\epsilon): \frac{\partial^2\psi_{10}}{\partial x^2} + \frac{\partial^2\psi_{10}}{\partial y^2} = -\Omega_{10}, \tag{17}$$

$$O(M^2): \frac{\partial^2\psi_{01}}{\partial x^2} + \frac{\partial^2\psi_{01}}{\partial y^2} = (\nabla\rho_{01}\cdot\nabla\psi_{00}) - \Omega_{01} - \rho_{01}\Omega_{10}, \tag{18}$$

$$O(\epsilon, M^2): \frac{\partial^2\psi_{11}}{\partial x^2} + \frac{\partial^2\psi_{11}}{\partial y^2} = (\nabla\rho_{01}\cdot\nabla\psi_{10}) + (\nabla\rho_{11}\cdot\nabla\psi_{00}) - \rho_{01}\Omega_{10} - \rho_{11}\Omega_{00}. \tag{19}$$

Similarly, the transport equation returns

$$O(M^4); \nabla\times(\boldsymbol{U}_{00}\times\boldsymbol{\Omega}_{01}) + \nabla\times(\boldsymbol{U}_{01}\times\boldsymbol{\Omega}_{00}) = (\nabla\rho_{01}\times\nabla p_{01}) = 0. \tag{20}$$

In the above, one may readily deduce that Eq. (20) vanishes inasmuch as the two vectors crossed on the right-hand side remain collinear. Only the relation for $\boldsymbol{\Omega}_{01}$ at $O(M^4)$ proves to be necessary, as Eq. (9) remains sufficient for the incompressible corrections; this may be attributed to the fact that, for an incompressible motion, the vorticity along a streamline remains constant.

As for the momentum equation, we collect

$$O(M^2) : \nabla p_{01} = -\gamma\Big[\nabla(\frac{\nabla\psi_{00}\cdot\nabla\psi_{00}}{2}) + \Omega_{00}\nabla\psi_{00}\Big], \tag{21}$$

$$O(\epsilon, M^2) : \nabla p_{11} = -\gamma\Big[\nabla(\nabla\psi_{00}\cdot\nabla\psi_{10}) + \Omega_{00}\nabla\psi_{10} + \Omega_{10}\nabla\psi_{00}\Big], \tag{22}$$

$$O(M^4) : \nabla p_{02} = -\gamma\Big\{\nabla(\nabla\psi_{00}\cdot\nabla\psi_{01}) - \nabla\Big[\rho_{01}(\psi_{00}\cdot\nabla\psi_{00})\Big] + \rho_{01}\nabla(\frac{\nabla\psi_{00}\cdot\nabla\psi_{00}}{2}) + \Omega_{00}\nabla\psi_{01} + \Omega_{01}\nabla\psi_{00}\Big\}. \tag{23}$$

Although the pressure correction at $O(\epsilon)$ is omitted, but is may be deduced straightforwardly using Bernoulli's equation for incompressible motion [4].

Lastly, the surface vorticity precipitates

$$O(1) : \Omega_{00} = \frac{\beta_{00}^2\psi_{00}}{y_s^2}, \tag{24}$$

$$O(\epsilon) : \Omega_{01} = \frac{\beta_{00}^2}{y_s^2}\psi_{10} + \frac{2\beta_{00}\beta_{10}}{y_s^2}\psi_{00} - \frac{\beta_{00}^2}{y_s^3}\psi_{00}. \tag{25}$$

s previously ascertained, the incompressibility of these first two terms enables us to substitute the vorticity and streamfunction into the surface vorticity relation such that a direct connection between the vorticity and streamfunction may be established. In so doing, the term involving $\beta'$ may be deliberately discounted, being a very small quantity according to Clayton [1].

Finally, the boundary conditions may be similarly expanded and segregated into successive orders, namely,

$$O(1) : \psi_{00}(x, y_s) = \psi_s, \quad \psi_{00}(x, 0) = 0, \quad \frac{\partial\psi_{00}}{\partial y}(0, y) = \frac{\pi}{2}L\ \cos(\frac{\pi}{2}y), \quad \frac{\partial\psi_{00}}{\partial x}(0, y) = 0, \tag{26}$$

$$O(\epsilon) : \psi_{10}(x, y_s) = 0, \quad \psi_{10}(x, 0) = 0, \quad \frac{\partial\psi_{10}}{\partial y}(0, y) = 0, \quad \frac{\partial\psi_{10}}{\partial x}(0, y) = 0, \tag{27}$$

$$O(M^2) : \psi_{01}(x, y_s) = 0, \quad \psi_{01}(x, 0) = 0, \quad \frac{\partial\psi_{01}}{\partial y}(0, y) = \rho_{01}\frac{\partial\psi_{00}}{\partial y}, \quad \frac{\partial\psi_{01}}{\partial x}(0, y) = \rho_{01}\frac{\partial\psi_{00}}{\partial x}, \tag{28}$$

$$O(\epsilon, M^2) : \psi_{11}(x, y_s) = 0, \quad \psi_{11}(x, 0) = 0, \quad \frac{\partial\psi_{11}}{\partial y}(0, y) = \rho_{11}\frac{\partial\psi_{00}}{\partial y}, \quad \frac{\partial\psi_{11}}{\partial x}(0, y) = \rho_{11}\frac{\partial\psi_{00}}{\partial x}. \tag{29}$$

# III. Solution

### A. Leading-Order Incompressible (Nontapered) Solution

By substituting Eq. (24) into Eq. (16), a second order linear partial differential equation (PDE) is obtained, specifically,

$$\frac{\partial^2\psi_{00}}{\partial y^2} + \frac{\beta_{00}^2\psi_{00}}{y_s^2} = 0. \tag{30}$$

Clayton [1] additionally determines that $\partial^2\psi/\partial x^2$ remains small, thus permitting its deliberate neglect without appreciable loss of accuracy. Next, by using separation of variables and applying the boundary conditions from Eq. (26), the leading-order streamfunction equation emerges. One gets

$$\psi_{00} = \psi_s \sin\Big(\beta_{00}\frac{y}{y_s}\Big); \quad \beta_{00} = \frac{\pi}{2}. \tag{31}$$

We hereby recover the same leading-order term as that reported by Saad et al. [4]. Moreover, by setting $L = \alpha = 0$, one recovers Taylor's profile for porous channels [2] as a special case that also matches the leading-order term in the work of Maicke and Majdalani [5]. With the leading-order streamfunction and vorticity now determined, Eqs. (24)

and (31) may be substituted into Eq. (21) to determine the $O(M^2)$ pressure correction. To further simplify the analysis, the terms $\beta_{00}$, $y$, and $y_s$ are grouped together as a new variable, $\eta$. Forthwith, integrating and substituting in the new variable yields a more compact expression, viz.

$$p_{01} = -\frac{\gamma}{2}\left[\left(\sec(\alpha)\ \sin(\eta) - \frac{\psi_s}{y_s}\eta\ \tan(\alpha)\ \cos(\eta)\right)^2 + \left(\frac{\psi_s\,\beta_{00}}{y_s}\right)^2\right]. \tag{32}$$

### B. First-Order Tapered Solution

Following a similar procedure, one may substitute Eq. (25) into Eq. (17) to produce

$$\frac{\partial^2\psi_{01}}{\partial y^2} + \frac{\beta_{00}^2\psi_1}{y_s^2} + \frac{2\beta_{00}\beta_{10}\psi_{00}}{y_s^2} - \frac{\beta_{00}^2\psi_{00}^2}{y_s^3} = 0. \tag{33}$$

The resulting PDE must be paired with the boundary conditions established in Eq. (27). After some effort, we retrieve

$$\psi_{10} = \frac{\psi_s}{6y_s}\left[3\psi_s + \psi_s\cos\left(2\frac{\beta_{00}y}{y_s}\right) - 2\psi_s\sin\left(\frac{\beta_{00}y}{y_s}\right) - 4\psi_s\cos\left(\frac{\beta_{00}y}{y_s}\right) + 6y\beta_{10}\cos\left(\frac{\beta_{00}y}{y_s}\right)\right]. \tag{34}$$

By setting the surface velocity $u_{s,10} = 0$ and substituting back into Eq. (34), one determines that $\beta_{10} = 2\psi_s/(3y_s)$,which is consistent with Saad et al. [4].

### C. Second-Order Tapered and Compressible Solution

To solve for $\psi_{01}$, one must first determine $\Omega_{01}$ through the vorticity transport equation. As $\Omega_{01}$ represents an extension of $\Omega_{00}$, one may posit an ansatz that retains the form $\Omega_{01} = \beta_{00}^2\psi_{01}/y_s^2 + \Omega_c$, where $\Omega_c$ must be ascertained through substitution back into the expanded form of Eq. (20). We have:

$$\frac{\partial}{\partial x}\left[\frac{\partial\psi_{00}}{\partial y}\Omega_{01} + \left(\frac{\partial\psi_{01}}{\partial y} - \rho_{01}\frac{\partial\psi_{00}}{\partial y}\right)\frac{\pi^2}{4}\psi_{00}\right] + \frac{\partial}{\partial y}\left[-\frac{\partial\psi_{00}}{\partial x}\Omega_{01} + \left(\rho_{01}\frac{\partial\psi_{00}}{\partial x} - \frac{\partial\psi_{01}}{\partial x}\right)\frac{\pi^2}{4}\psi_{00}\right] = 0. \tag{35}$$

Since all other terms have been determined, one may integrate the resulting PDE to obtain

$$\Omega_{01} = \frac{\beta_{00}^2}{y_s^2}\psi_{01} + \beta_{00}^2\left(1 - \frac{1}{y_s}\right)\psi_{01} + \frac{\beta_{00}^2}{y_s^2}\rho_{01}\psi_{00} + f(\psi_{00}). \tag{36}$$

In the resulting approximation, $f(\psi_{00})$ denotes an arbitrary function that will be set when solving $\psi_{01}$ to help enforce the boundary conditions. With $\Omega_{01}, \Omega_{00}, \psi_{00}$, and $p_{01}$ in hand, Eq. (18) can be tackled successfully. To begin, we follow Maicke and Majdalani [11] by expressing the general solution in the form of

$$\psi_{01}(x,\eta) = xG(\eta) + x^3H(\eta), \tag{37}$$

where the underlying dependence on odd powers of $x$ has been established in two previous compressible-flow investigations of injection-driven flows [11, 12]. Following the ansatz for the general solution in a porous channel, the form for $f(\psi_{00})$ can be taken to be

$$f(\psi_{00}) = A_1x\ \sin(\eta) + A_2x^3\ \sin(\eta). \tag{38}$$

These enable us to solve for $G(\eta)$ and $H(\eta)$, which, when subjected to the constraints in Eq. (28), yield

$$\psi_{01} = x\left[\left(\frac{1-3\pi^2}{16}\right)\sin\eta + \eta\cos\eta + \frac{\sin(3\eta)}{16} + \frac{3\eta^2\sin\eta}{4}\right] - \frac{\pi^2x^3}{8}\eta\ \cos(\eta). \tag{39}$$

Subsequently, by expanding the terms in Eq. (22) while ignoring $\partial^2\psi/\partial x^2$ as performed by Clayton [1], integration enables us to retrieve

$$p_{11} = -\frac{\gamma\pi^2\psi_s^3}{24y_s^3}\left[2\sin^3\left(\frac{\pi y}{2y_s}\right) + \cos^2\left(\frac{\pi y}{2y_s}\right) - 2\right]. \tag{40}$$

### D. Third-Order Tapered and Compressible Solution

Having determined $p_{01}$, $\psi_{10}$, $\Omega_{10}$, $\Omega_{00}$, and $p_{11}$, Eqs. (24), (25), (31), (32) and (34) may be inserted into Eq. (19) to deduce the final streamfunction correction, $\psi_{11}$. By availing ourselves to Clayton's approximationClayton [1], expanding the right-hand-side of Eq. (19), integrating, and then securing the boundary conditions specified by Eq. (29), we finally arrive at:

$$\psi_{11} = -\frac{\pi^2 \psi_s^4}{24 y_s^3}\left[\left(\frac{8}{\pi}-1\right)\cos\eta + \frac{1}{3}\cos^3\eta - \left(\frac{8}{\pi}-\frac{2}{3}\right)\left(1-\frac{2\eta}{\pi}\right)\right]. \tag{41}$$

With everything else determined, one may now proceed to solve Eq. (23) so as to determine the final pressure correction. Due to the complexity associated with solving for this term, an approximation is deliberately introduced such that $\Omega_{01}\nabla\psi_{00} = \psi_{01}\nabla\Omega_{00}$; this equality allows us to group gradient terms in a manner that substantially simplifies the ensuing analysis. While this equality remains only approximate (due to some minor terms arising from the taper), these will be treated as higher-order contributions that have a minimal bearing on the solution. The last term in our expansion emerges as:

$$\begin{aligned}
C_4 &= \frac{1-3\pi^2}{16}, \\
G &= C_4 \sin\eta + \eta\cos\eta + \frac{\sin(3\eta)}{16} + \frac{3\eta^2\sin\eta}{4} - \frac{\pi^2 x^3 \eta\cos\eta}{8}, \\
G_\eta &= (C_4+1)\cos\eta - \eta\sin\eta + \frac{3\cos(3\eta)}{16} + \frac{3\eta^2\cos\eta}{4} + \frac{3\eta\sin\eta}{2} - \frac{\pi^2 x^3}{8}(\cos\eta - \eta\sin\eta), \\
p_{02} &= \sin\eta\, G\,(\beta_{00}^2 L x - \gamma) - \gamma L x \beta_{00}^2 \cos\eta\, G_\eta + \frac{3\gamma\pi^2 x^3 \eta \sin\eta\cos\eta}{8} \\
&\quad - \gamma\left[\frac{(1+L^2\beta_{00}^2)^2}{8\beta_{00}^2} - \frac{L^2\beta_{00}^2(1+3L^2\beta_{00}^2)}{32\beta_{00}^2}\right] \\
&\quad - \gamma\left[\frac{L^4\beta_{00}^4 - 1 + L^2\beta_{00}^2}{4} + \frac{L^2\beta_{00}^2}{8}\right]\cos(2\eta) \\
&\quad - \gamma\left[\frac{(L^2\beta_{00}^2-1)^2}{16} + \frac{L^2\beta_{00}^2(L^2\beta_{00}^2-1)}{32}\right]\cos(4\eta).
\end{aligned} \tag{42}$$

## IV. Results and Discussion

With the streamfunction and pressure corrections now determined, one may proceed to examine the effects of taper and compressibility on the flowfield within the chamber. As the $O(1)$ and $O(\epsilon)$ terms remain identical to those reported by Saad et al. [4], the truly distinctive corrections emerge at $O(M^2)$, $O(\epsilon M^2)$; for the pressure and density fields, these appear at $O(M^4)$. In contrast to $\psi_{01}$ derived by Maicke and Majdalani [5], the $\psi_{01}$ obtained in this study remains a function of the first two taper corrections; it hence incorporates the $y_s$ term in its $\eta$, which differs from the $\eta$ in the previous work that depends solely on $y$. This distinction is further manifested in the higher-order $p_{11}$, $\psi_{11}$, and $p_{02}$ terms, which are also functions of the taper corrections, albeit serving as compressible perturbations themselves.

### A. Streamlines

To visualize the manner in which the streamfunction evolves under the combined effects of compressibility and taper corrections, the streamlines through the chamber are plotted for a baseline case, a zero-taper case, and an incompressible case. The Mach number and taper angle $\alpha$ are selected to be representative of typical SRM conditions. Comparing first Figs. 2a and 2b, the compressibility effects become more pronounced with increasing axial distance down the chamber. The rapid turning induced by compressibility, as previously noted by Maicke and Majdalani [5], is also readily observed between these two plots. Among Figs. 2a, 2b and 3, the effect of the taper on the solution is captured with remarkable fidelity. In contrast to the nontapered solution, the streamlines in both tapered configurations begin to deflect upwards as the chamber expands. The tapered corrections appear to provide the largest contributions, as the disparity between the two compressible solutions is markedly sharper than that between the two tapered solutions. These observations help to ascertain the importance of accurately capturing the taper effect when modeling SRMs.

**Table 1. Stream Function and Density Corrections Sorted by Perturbation Order**

| Order | Variable | Expression |
|---|---|---|
| $O(1)$ | $\psi_{00}$ | $\psi_s \sin\left(\beta_{00}\dfrac{y}{y_s}\right), \quad \beta_{00} = \dfrac{\pi}{2}$ |
| $O(\epsilon)$ | $\psi_{10}$ | $\dfrac{\psi_s}{6y_s}\left[3\psi_s + \psi_s\cos^2\eta - 2\psi_s\sin\eta - 4\psi_s\cos\eta + 6y\beta_{10}\cos\eta\right], \quad \beta_{10} = \dfrac{2\psi_s}{3y_s}$ |
| $O(M^2)$ | $\psi_{01}$ | $x\left[\left(1 - \dfrac{3\pi^2}{16}\right)\sin\eta + \eta\cos\eta + \dfrac{\sin 3\eta}{16} + \dfrac{3\eta^2\sin\eta}{4}\right] - \dfrac{\pi^2 x^3}{8}\eta\cos\eta$ |
| $O(M^2)$ | $\rho_{01}$ | Obtained via $\rho = p^{1/\gamma}$ from $p_{01}$, see Eq. (32) |
| $O(\epsilon M^2)$ | $\psi_{11}$ | $-\dfrac{\pi^2\psi_s^4}{24y_s^3}\left[\left(\dfrac{8}{\pi} - 1\right)\cos\eta + \dfrac{1}{3}\cos 3\eta - \left(\dfrac{8}{\pi} - \dfrac{2}{3}\right)\left(1 - \dfrac{2\eta}{\pi}\right)\right]$ |
| $O(\epsilon M^2)$ | $\rho_{11}$ | Obtained via $\rho = p^{1/\gamma}$ from $p_{12}$; see Eq. (40) |
| $O(M^4)$ | $\rho_{02}$ | Obtained via $\rho = p^{1/\gamma}$ from $p_{02}$; see Eq. (**??**) |

$\eta \equiv \beta_{00}\, y/y_s;\quad y_s = 1 + x\tan\alpha;\quad \psi_s = x\sec\alpha + L$

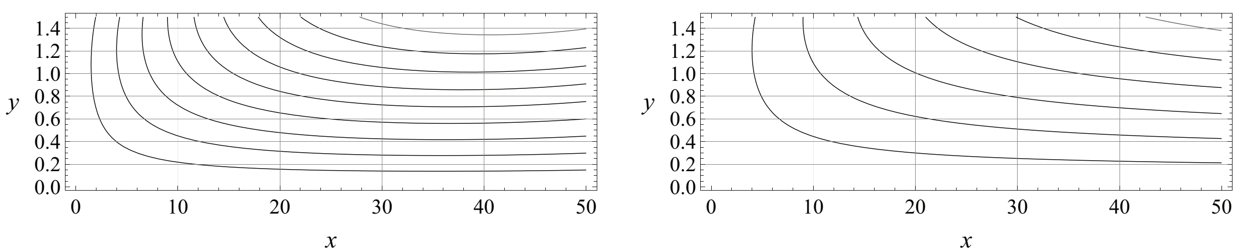

a) b)

**Fig. 2. Streamlines corresponding to a) compressible and tapered motor for $M = 0.01$ and b) incompressible and tapered slab motor. Unless specified otherwise, the taper divergence half angle is taken to be $\alpha = 3^{\circ}$.**

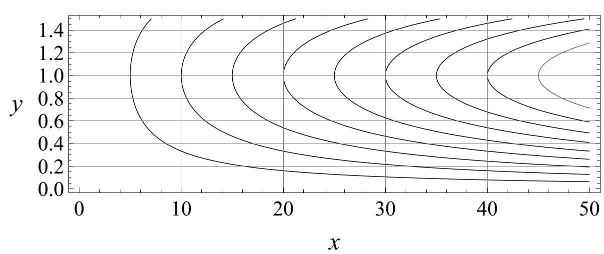

**Fig. 3. Compressible streamlines for the nontapered slab motor for $M = 0.01$.**

## B. Axial Velocity

By expanding the definition of the axial velocity,

$$u = \frac{1}{\rho} \frac{\partial \psi}{\partial y}, \tag{43}$$

and by invoking the relation given by Eq. (6), the axial velocity throughout the chamber may be determined using the asymptotic corrections. To visualize this, the axial velocity is plotted in Fig. 4 at four axial stations corresponding to $x = \{5, 10, 15, 20\}$, across the chamber length. As was done with the streamlines, the axial velocity is characterized for a baseline compressible and tapered case (Fig. 4a), an incompressible tapered case (Fig. 4b), and a compressible nontapered case (Fig. 5).

Similar to the streamlines, the compressibility effects become more prominent with increasing axial distance down the chamber bore, with the velocity profiles appearing nearly identical at $x = 5$ and $x = 10$. The corrections also exhibit increasing strength as the axial distance is increased. Compared to the tapered cases, the nontapered configuration in Fig. 5 produces higher velocities. This observation aligns with the findings of Saad et al. [4], wherein relaxing the taper angle leads to generally higher velocities at the same axial locations. Such behavior may also be attributed to mass conservation, as for subsonic flows, an increase in the cross-sectional area will invariably cause the flow speed to decrease.

# V. Conclusions

In this work, a closed-form, four-term analytical solution is derived for the streamfunction and density fields in an idealized tapered slab rocket motor subject to compressible, inviscid, steady, and isentropic flow conditions. By jointly expanding the governing equations in the small taper parameter, $\epsilon = \sin\alpha$, and the injection Mach number squared, $M^2$, a unified asymptotic framework is established that systematically incorporates both geometric divergence and dilatational effects. This double perturbation procedure constitutes a natural extension of the classical Rayleigh–Janzen technique that allows grain taper and compressibility corrections to be treated concurrently within a consistent vorticity–streamfunction formulation.

At leading order, the solution reduces to the incompressible Taylor profile in a tapered chamber, thereby recovering the classical rotational mean flow structure. Higher-order terms help to quantify the progressive effects of compressibility and taper on the velocity, pressure, density, and vorticity distributions. On the one hand, the $O(M^2)$ and $O(\epsilon M^2)$ corrections are found to prescribe the manner in which dilatational effects intensify axial velocity gradients and redistribute pressure along the chamber; on the other hand, the $O(\epsilon)$ terms enable us to capture the geometric deflection induced by wall divergence.

The streamline topology and axial velocity distributions confirm the necessity of accounting for both perturbations in high-speed solid rocket motors. Compressibility effects become increasingly pronounced with downstream distance,

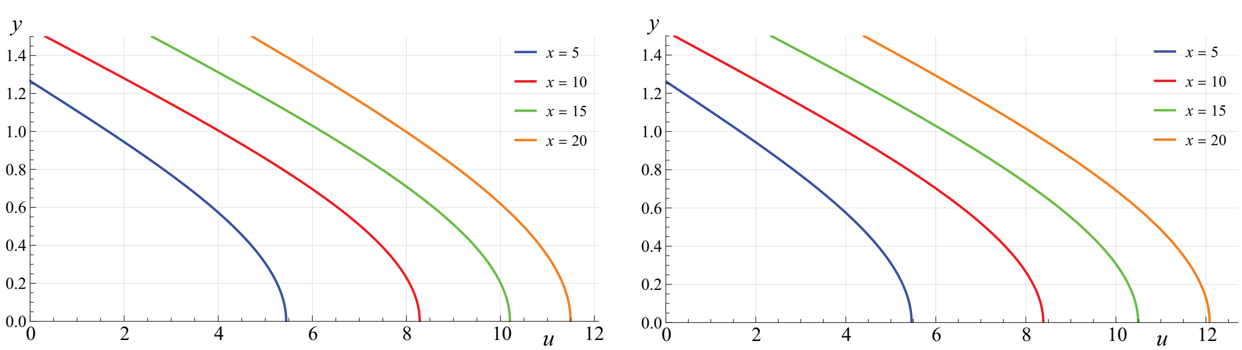


**Fig. 4. Axial velocity distributions corresponding to a) compressible and tapered motor for $M = 0.01$ and b) incompressible and tapered slab motor. Results are shown at four evenly spaced axial stations using $x = 5, 10, 15$ and 20. Here too, the taper divergence half angle is taken to be $\alpha = 3^{o}$.**

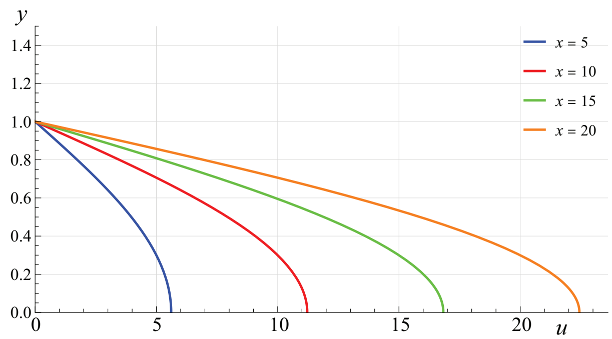


**Fig. 5. Axial velocity at various locations for nontapered motors.**

with discernible deviations emerging beyond $x \approx 10$ (nondimensionalized by the half-channel height $h_0$). In elongated or slender chambers, neglecting compressibility may therefore lead to appreciable underprediction of axial velocity and associated pressure gradients.

Similarly, taper effects can be appreciable in modifying the global flow structure. The divergent geometry induces an upward deflection of streamlines that is absent in nontapered configurations. Consistent with mass conservation in subsonic flow, the tapered chamber exhibits reduced axial velocities relative to its parallel-wall counterpart, as the gradual increase in cross-sectional area mitigates streamwise accelerations. These findings align with prior incompressible tapered analyses while demonstrating that compressibility further modulates this behavior in high-speed regimes.

By synthesizing the geometric corrections of tapered configurations with the dilatational corrections of compressible injection-driven flow, the present solution combines the contributions identified in two previously independent lines of investigation. The results help to identify the limitations of ballistic models that neglect either taper or compressibility, particularly in modern motors characterized by slight grain divergence and non-negligible injection Mach numbers.

Overall, the present analysis confirms that the relative importance of each correction depends on the particular chamber geometry and operating conditions. While compressibility effects may remain secondary in relatively thick or short channels, taper corrections are generally indispensable in divergent configurations. Conversely, in long, slender motors operating at elevated injection speeds, such as those associated with interceptor motors, dilatational effects become increasingly significant. The unified formulation presented herein provides a more comprehensive analytical foundation for improving ballistic predictions and for guiding future computational and experimental investigations of high-speed SRM internal flows.

## References


[1] Clayton, C., "Flowfields in Solid Rocket Motors With Tapered Bores," *AIAA, ASME, SAE, and ASEE, Joint Propulsion Conference and Exhibit, 32nd*, AIAA Paper 96-2643, Lake Buena Vista, FL, 1996. doi:10.2514/6.1996-2643.

[2] Taylor, G. I., "Fluid Flow in Regions Bounded by Porous Surfaces," *Proceedings of the Royal Society of London. Series A. Mathematical and Physical Sciences*, Vol. 234, No. 1199, March 1956, pp. 456–475. doi:10.1098/rspa.1956.0050.

[3] Culick, F. E. C., "Rotational Axisymmetric Mean Flow and Damping of Acoustic Waves in a Solid Propellant Rocket," *AIAA Journal*, Vol. 4, No. 8, August 1966, pp. 1462–1464. doi:10.2514/3.3709.

[4] Saad, T., Sams, O. C., and Majdalani, J., "Rotational Flow in Tapered Slab Rocket Motors," *Physics of Fluids*, 2006.

[5] Maicke, B. A. and Majdalani, J., "On The Compressible Bidirectional Vortex," *44th AIAA/ASME/SAE/ASEE Joint Propulsion Conference and Exhibit*, AIAA Paper 2008-4834, July 2008. doi:10.2514/6.2008-4834.

[6] Janzen, O., "Beitrag zu Einer Theorie der Stationären Strömung Kompressibler Flüssigkeiten," *Physikalische Zeitschrift*, 1913.

[7] Rayleigh, L., "On the Flow of a Compressible Fluid Past an Obstacle." *Philosophical Magazine*, 1916.

[8] Flandro, G. A., "Stability Prediction for Solid Propellant Rocket Motors with High-Speed Mean Flow," Final Technical Report AFRPL-TR-79-98, Air Force Rocket Propulsion Laboratory, Edwards AFB, CA, 1980.

[9] Majdalani, J., "The Compressible Taylor–Culick Flow," *41st AIAA/ASME/SAE/ASEE Joint Propulsion Conference and Exhibit*, No. AIAA Paper 2005-3542, 2005. doi:10.2514/6.2005-3542.

[10] Majdalani, J., "On Steady Rotational High Speed Flows: The Compressible Taylor–Culick Profile," *Proceedings of the Royal*

*Society of London, Series A*, Vol. 463, 2007, pp. 131–162. doi:10.1098/rspa.2006.1755.

[11] Maicke, B. A. and Majdalani, J., "On the Rotational Compressible Taylor Flow in Injection-Driven Porous Chambers," *Journal of Fluid Mechanics*, Vol. 603, No. 5, 2008, pp. 391–411. doi:10.1017/S0022112008001122.

[12] Majdalani, J., "On Steady Rotational High Speed Flows: The Compressible Taylor-Culick Profile," *Proceedings of the Royal Society, London, Series A*, Vol. 463, No. 2077, 2007, pp. 131–162. doi:10.1098/rspa.2006.1755.